Northumbria University NEWCASTLE

CUSTOMER SERVICE EXCELLENCE

University Library

Temperate rainforests near the South Pole during peak Cretaceous warmth

Klages, J.P.[1], Salzmann, U.[2], Bickert, T.[3], Hillenbrand, C.-D.[4], Gohl, K.[1], Kuhn, G.[1], Bohaty, S.[5], Titschack, J.[3,6], Müller, J.[1,7], Frederichs, T.[7], Bauersachs, T.[8], Ehrmann, W.[9], van de Flierdt, T.[10], Simões Pereira, P.[10+], Larter, R.D.[4], Lohmann, G.[1,3,11], Niezgodzki, I.[1,12], Uenzelmann-Neben, G.[1], Zundel, M.[7], Spiegel, C.[7], Mark, C.[13++], Chew, D.[13], Francis, J.E.[4], Nehrke, G.[1], Schwarz, F.[2], Smith, J.A.[4], Freudenthal, T.[3], Esper, O.[1], Pälike, H.[3], Ronge, T.[1], Dziadek, R.[1], and the Science Team of Expedition PS104[‡]*

[1] Alfred-Wegener-Institut Helmholtz-Zentrum für Polar- und Meeresforschung, Bremerhaven, Germany
[2] Northumbria University, Department of Geography and Environmental Sciences, Newcastle upon Tyne, United Kingdom
[3] MARUM – Center for Marine Environmental Sciences, Bremen, Germany
[4] British Antarctic Survey, Cambridge, United Kingdom
[5] School of Ocean and Earth Science, University of Southampton, Southampton, United Kingdom
[6] Senckenberg am Meer (SAM), Marine Research Department, Wilhelmshaven, Germany
[7] University of Bremen, Faculty of Geosciences, Bremen, Germany
[8] Christian-Albrechts-University, Institute of Geoscience, Kiel, Germany
[9] University of Leipzig, Institute for Geophysics and Geology, Leipzig, Germany
[10] Imperial College London, Department of Earth Science & Engineering, London, United Kingdom
[11] University of Bremen, Environmental Physics, Bremen, Germany
[12] ING PAN – Institute of Geological Sciences, Polish Academy of Sciences, Biogeosystem Modelling Laboratory, Kraków, Poland
[13] Department of Geology, Trinity College Dublin, Dublin, Ireland
[+] now at: University of Gothenburg, Department of Marine Sciences, Gothenburg, Sweden
[++] now at: School of Earth Sciences, University College Dublin, Dublin, Ireland
[‡] A full list of authors and their affiliations appears at the end of the paper
* Corresponding author: Johann.Klages@awi.de

The mid-Cretaceous was one of the warmest intervals of the past 140 million years (Myr)[1–5] driven by atmospheric CO_2 levels around 1000 ppmv[6]. In the near absence of proximal geological records from south of the Antarctic Circle, it remains disputed whether polar ice could exist under such environmental conditions. Here we present results from a unique sedimentary sequence recovered from the West Antarctic shelf. This by far southernmost Cretaceous record contains an intact ~3 m-long network of *in-situ* fossil roots. The roots are embedded in a mudstone matrix bearing diverse pollen and spores, indicative of a temperate lowland rainforest environment at a palaeolatitude of ~82°S during the Turonian–Santonian (92–83 Myr). A climate model simulation shows that the reconstructed temperate climate at this high latitude requires a combination of both atmospheric CO_2 contents of 1120–1680 ppmv and a vegetated land surface without major Antarctic glaciation, highlighting the important cooling effect exerted by ice albedo in high-CO_2 climate worlds.

The Cretaceous Period (144–66 Myr) hosted some of the warmest intervals in Earth's history[1–3], particularly during its Turonian to Santonian stages (93.9–83.6 Myr)[4,5]. At that time, atmospheric carbon dioxide (CO_2) concentrations were reconstructed to be around 1000 ppmv[6], and average annual low latitude sea surface temperatures probably reached ~35°C[4], with only a minor bi-hemispheric temperature gradient extending poleward from palaeo-latitudes between 50-60°N (refs. 7–9). Only small to medium-sized ice sheets may have existed[10,11] and global sea level was up to 170 m higher than at present[11,12].

Records documenting the Antarctic terrestrial environment during mid-Cretaceous warmth are sparse[5,13–17] and particularly rare south of the palaeo-Antarctic Circle[13,14]. Such records, however, are critical to constrain state-of-the-art Late Cretaceous climate models[5] for predicting the magnitude of atmospheric CO_2 concentrations[18] and their effectiveness in inhibiting the build-up of major ice sheets[19].

Here we reconstruct mid-Cretaceous terrestrial environmental conditions in West Antarctica by combining micro- and macropalaeontological, sedimentological, inorganic and organic geochemical, mineralogical, and palaeomagnetic data as well as X-ray computed tomography (CT) imagery obtained from drill cores recovered from a site within the Pine Island cross-shelf trough in the Amundsen Sea Embayment (ASE), West Antarctica (Fig. 1a). Site PS104_20-2 (73.57°S, 107.09°W; 946 m water depth) was drilled during RV *Polarstern* expedition PS104 in 2017 (ref. 22). The Pine Island Trough extends from the modern fronts of Pine Island and Thwaites glaciers, and was eroded into the ASE shelf during repeated advances of a West Antarctic Ice Sheet (WAIS) palaeo-ice stream throughout Miocene–Pleistocene epochs[23–25]. On the inner–middle continental shelf, glacial erosion combined with tectonic uplift[24] exposed seaward-dipping sedimentary strata of postulated Cretaceous to Miocene age near the seafloor[26] (Fig. 1b). Widespread till cover on the shelf previously prevented sampling of these strata using conventional coring techniques[26]. Deployment of the remotely operated seafloor drill rig *MARUM-MeBo70* (ref. 27) enabled drilling to 30.7 metres below sea floor (mbsf) into the seabed and recover the dipping strata[22] (Figs. 1, 2).

Lithology and stratigraphy

Beneath a few meters of glacimarine and reworked glacial sediments, *MARUM-MeBo70* penetrated occasionally stratified but microfossil-barren ca. 17 to 24 m-thick quartzitic sandstone with uranium/lead (U/Pb) dates on apatite and zircon grains (see Methods) constraining its maximum depositional age to ~40 Myr in the late Eocene (Extended Data Fig. 1). Cores 9R and 10R recovered strata from 26.3 mbsf to the base of the hole. At ca. 26.8 mbsf, a prominent 5 cm thin layer of indurated lignite fragments separates the overlying sandstone unit from a ≥3 m-thick palynomorph-rich, laminated to stratified carbonaceous mudstone below. This mudstone contains an intact and continuous network of fossil plant roots that reaches down to at least ~30 mbsf (Fig. 2; Supplementary Video 1).

Based on New Zealand's biostratigraphic ranges[28], the presence of the pollen taxon *Phyllocladites mawsonii* (Nearest Living Relative (NLR): *Lagarostrobos*, Huon Pine) and the absence of both *Nothofagidites* (NLR: *Nothofagus*, Southern Beech) and *Forcipites sabulosus* within the carbonaceous mudstone indicate its deposition during the mid-Cretaceous (Turonian–Santonian; ~92–83 Myr, PM1a-subzone) (Extended Data Fig. 2; Extended Data Tables 1, 2). Abundant pollen of conifer trees (e.g. *Podocarpidites*, *Trichotomosulcites*), tree ferns (*Cyathidites*), and the presence of accessory taxa such as *Ruffordiaspora ludbrookiae* and *Tricolpites* spp. in our assemblage resemble the uppermost strata of the Turonian–Santonian Tupuangi Formation on Pitt Island, New Zealand, dated to 92-89 Myr[29,30] (Extended Data Table 3). However, the regular occurrence of pollen of the family Proteaceae, including *Beauprea*-type pollen (e.g. *Peninsulapollis gilii*, *Beaupreaidites*), which are absent from the Tupuangi Formation, suggest the ASE core to be slightly younger than 89 Myr. Recent molecular phylogenetic reconstructions indicate an early Antarctic-Southeastern Australian origin of *Beauprea* (~88 Myr ago), while the oldest palynological record of these angiosperm fossils on Antarctica and Australia date back to 81.4 Myr and 83.8 Myr, respectively[31].

These biostratigraphic age estimates are consistent with palaeomagnetic data obtained from discrete sediment samples showing normal polarity, expected for deposition during the 'Cretaceous Normal Polarity Superchron' (C34n; 121–83 Myr; ref. 32) (see Methods). The layer of indurated lignite and the underlying carbonaceous mudstone show very similar pollen assemblages, which indicate a similar age and palaeoenvironment for both units (Fig. 2; Extended Data Fig. 2).

Turonian–Santonian position of the record

In order to assess the palaeoclimatic significance of this record, we determined the palaeogeographical position of site PS104_20-2 at 90 Myr. Today, the site is located near the Pacific continental margin of West Antarctica about 250 km away from the modern boundary between continental and oceanic crust (Fig. 1). At the time of sediment deposition between 93 and 83 Myr, the continent of Zealandia started to rift and separate from West Antarctica[33,34]. We applied a relative plate reconstruction between Zealandia and West

Antarctica for the middle Cretaceous using the *GPlates* plate reconstruction tool[35] with up-to-date rotation parameters of the South Pacific realm[33]. This resulted in a 736-km great-circle distance (265 km North-South distance) between the drill site and the hitherto southernmost mid-Cretaceous terrestrial palaeoenvironmental record on Pitt Island on Chatham Rise, New Zealand[14]. The close fit reconstruction at 90 Myr indicates a wide rift zone between Zealandia and West Antarctica, just before initiation of the continental breakup[26,33]. In a previous study[36], a 100-Myr mean palaeomagnetic pole position of 75.7°S and 135.9°W with a 95% confidence radius of 3.8° for Marie Byrd Land was determined from 19 rock sample sites. By accounting for the great-circle distance of 7.84° to our drill site and rotating points on the East Antarctic polar wander path[36] into the Marie Byrd Land reference frame, we derive a core site palaeolatitude of 81.9°S at 90 Myr. Its uncertainty is estimated to be not larger than the maximum 95% confidence radius of 5.9° of the respective part of the polar wander path[36].

Palaeoenvironment

The indurated lignite layer as well as the laminated to stratified carbonaceous mudstone comprising the fossil plant roots in cores 10R and lower 9R at site PS104_20-2 contain a highly diverse and entirely terrestrial palynomorph assemblage of more than 62 pollen and spore taxa (Fig. 2; Extended Data Figs. 2, 3; Extended Data Table 3). The absence of palynomorphs with different stratigraphic ranges or varying thermal maturity suggests that this purely terrestrial microfossil assemblage has not been reworked. The assemblage is dominated by pollen of the conifer tree families Podocarpaceae and Araucariaceae with abundant ferns, including the tree ferns *Cyathea*, documenting the initial stages of an Austral temperate rainforest (Fig. 2; Extended Data Fig. 2; Extended Data Table 2). The presence of the heterocyst glycolipids HG_{30} triol and keto-diol (Extended Data Fig. 4; see Methods) also indicates that benthic cyanobacterial mats colonized fresh water bodies within this temperate rainforest, providing additional evidence for the development of a highly complex ecosystem in the ASE during the Turonian–Santonian. In combination with published palaeo-topographic and palaeo-tectonic information[24,26,33,34], the different taxa and their bioclimatic significance (see Methods) were combined and visualized to create Fig. 4. Members of the Proteaceae family presumably formed a flowering shrub understorey in the tall Late Cretaceous conifer rainforest of the ASE depicted in Fig. 4. The lignite layer is rich in spores of *Stereisporites antiquasporites* (NLR: Bryophyte, *Sphagnum*), which further suggest the temporary existence of a peat swamp in the diverse temperate lowland rainforest. This coincides with increasing *Peninsulapollis* pollen indicating increasing humidity[37] towards the record's top. Thin sections were carefully prepared from resin-impregnated core samples selected from cores 9R and 10R (see Methods) to characterize the fossil roots. Although cell structures were not sufficiently preserved for identification of the plant that grew the roots, the presence of parenchyma cells within the long and continuous roots likely identifies the network as vascular plant remains and thus confirms active plant growth at our site (Extended Data Fig. 5b–e). Further, the alignment of organic and clastic material within the laminated to stratified mudstone matrix (Extended Data Fig. 5a) suggests synchronous deposition of clastic particles and organic fragments.

Our environmental reconstruction is further supported by geochemical and biomarker data. In the mudstone between 29.80 and 27.03 mbsf and the indurated lignite interval (26.83–26.77 mbsf), absent to very low halite and carbonate contents in the bulk sediment fraction combined with low total organic carbon/total nitrogen (TOC/TN) ratios and low ratios of higher land-plant-derived long-chain *n*-alkanes versus aquatic-sourced short-chain *n*-alkanes (TAR) point to swampy aquatic freshwater conditions (Fig. 2). This interpretation is supported by the identification of cells closely resembling aerenchyma (Extended Data Fig. 5d) usually being responsible for inter-cellular gas exchange under (semi-) permanent subaquatic growing conditions[38]. In mudstone samples taken from the core segment containing a particularly dense root network (27.03–26.83 mbsf), pollen and biomarkers indicate the establishment of terrestrial forest-type vegetation, whilst elevated pristane/n-C_{17} and pristane/phytane ratios point to high abundance of terrigenous plant material (Extended Data Fig. 6; cf. refs. 39, 40), which is in line with the pollen-based interpretation of a terrestrial rainforest environment. TOC/TN ratios >20 (Fig. 2) are consistent with this interpretation and indicate a primarily land plant source of organic matter[41] within this mudstone sequence. The clay mineral assemblage in cores 9R and 10R is dominated by kaolinite (67–72%) and smectite (26–29%), both indicating chemical weathering activity under humid and (sub-) tropical climate conditions[42]. However, as this is not corroborated by our reconstructed climatic setting, we attribute kaolinite formation in the mudstone predominantly to the establishment of repeated swampy conditions, in which organic acids altered silicate minerals to kaolinite (= 'Moorverwitterung')[43].

The lithological succession in cores 9R and 10R resemble the uppermost strata of the Turonian–Santonian Tupuangi Formation on Pitt Island, New Zealand[29]. The Pitt Island strata are characterized by interbedded carbonaceous siltstone, quartzo-feldspathic sandstone and lignite and/or peat layers. Similar to the sediment sequence described for the ASE, the Tupuangi Formation records a terrestrial, densely vegetated, and partly swampy fluviodeltaic environment[14]. Some 90 million years ago, the Tupuangi Formation was located in one of the rift basins developing before Zealandia separated from West Antarctica[26,33], ~736 km away from Site PS104_20-2 (Fig. 1). A diverse conifer forest surrounded by extensive river systems[44,45] appears to have covered both the Zealandian[14] and the West Antarctic conjugate continental margin during this early break-up phase.

The sharp lithological change from the fossil root-bearing mudstone with the thin layer of indurated lignite on top into the sandstone at 26.77 mbsf is marked by increased iron carbonate and halite contents and decreased TOC/TN and TAR ratios within the sandstone (Fig. 2), suggesting an estuarine and coastal environment. The U/Pb dates of max. ~40 Myr obtained from the sandstone (see Extended Data Fig. 1), which is coarse-grained at its base, indicate a significant hiatus between the mudstone (including the lignite) and the sandstone. Such a hiatus is consistent with neodymium (Nd) and strontium (Sr) isotope data, reflecting both a change in sediment provenance and a decrease in weathering intensity between the two lithologies (Fig. 2; see Methods). The time window of the hiatus coincides with slow erosion rates of a tectonically quiescent passive margin[24,46], whereas Eocene/Oligocene tectonic activity of the West Antarctic Rift System might have triggered renewed sedimentation of dominantly clastic material[46,47].

Palaeoclimate

Multi-proxy evidence from our mid-Cretaceous sedimentary record reveals an environment at a palaeolatitude of ~82°S on the Antarctic continental margin that was characterised by a regional temperate climate warm enough to maintain a diverse temperate rainforest (Fig. 4) only ~900 km away from the palaeo-South Pole. Our palynomorph-based climate reconstruction based on the approach outlined in ref. 48 indicates mean annual temperatures of 13°C with precipitation around 1,120 mm/year. The temperature of the warmest summer month was around 18.5°C on average. Previous quantitative climate analyses from Antarctic records ~2,500 km further north resulted in late Coniacian–early Santonian mean annual temperatures of 15–21°C[49,50], suggesting a shallow gradient to our site. NLR-based estimates of Late Cretaceous climate generally agree well with other temperature proxies[49]. However, the approach assumes similarity of climate requirements for fossil taxa and their NLRs. As with increasing age the phylogenetic relationships of a fossil taxon become more disparate, the assumption becomes less robust. We therefore applied an independent geochemical palaeothermometer based on heterocyst glycolipid distribution (HTI_{30})[51], which corroborated our bioclimatic reconstructions by indicating austral summer lake or river-surface temperatures of ~20°C for the swampy rainforest (Extended Data Fig. 4; see Methods). Our record contains the hitherto southernmost evidence of Cretaceous terrestrial environmental conditions and reveals a mid-Cretaceous 'greenhouse climate' that was capable of maintaining temperate conditions much further south than previously documented[14].

Palaeoclimate modelling

In light of extremely limited mid-Cretaceous CO_2 proxy data[6] and widely scattered existing data estimates[5] and in order to identify some of the pivotal driving mechanism of high-latitude mid-Cretaceous environmental conditions reconstructed for our new record, we ran the global climate model COSMOS[5] in a coupled atmosphere–ocean configuration with fixed vegetation. We did so under present (Fig. 3a-c) and mid-Cretaceous configurations at 90 Myr (Fig. 3d-g) for 1x, 2x, 4x and 6x pre-industrial CO_2 levels of 280 ppm (280, 560, 1120 and 1680 ppmv, respectively; see Methods). Although the model predicts a mid-Cretaceous climate in West Antarctica that is already warmer under pre-industrial CO_2 levels of 280 ppm (Fig. 3d), summer surface air and water temperatures of ~20°C at ~82°S can only be reproduced by forcing the climate with very high atmospheric CO_2 levels between 1120 and 1680 ppmv (Fig. 3f, g). Our reconstructed mean annual temperature of 13°C, however, still remains significantly underestimated by the model (Fig. 3g).

We conclude that a temperate climate at such a high latitude with more than four months of complete polar night darkness requires a combination of both strongly elevated atmospheric CO_2 concentrations and dense surface vegetation that generates a low planetary albedo with an associated high radiant energy absorption and pronounced seasonality. This largely excludes the existence[10] of any substantial ice-sheet and sea-ice cover in and around Antarctica during the Turonian to Santonian stages of the Late Cretaceous epoch, likely additionally favoured by palaeo-geographic variations[52]. Conversely, the present Antarctic Ice Sheet and its associated climate feedbacks, such as the ice albedo, provide a stabilizing cooling effect in a future high-CO_2 world (Fig. 3a-c).

To further elaborate on the significance of additional forcing mechanisms, to discover the interdependency of surface vegetation and temperature sensitivity in more detail, and to explore the drivers of the late Cretaceous latitudinal gradient paradox visible in Fig. 3, future work will aim at running the model with various types of vegetation cover coupled with other drivers such as palaeo-geography[52] or changes in cloudiness[53].

Our findings highlight the importance of including land–ice changes into long-term climate simulations in order to accurately estimate climate sensitivity on these extended time scales[54]. We provide new key data for constraining the response of polar terrestrial ecosystems to very high atmospheric CO_2 concentrations and for assessing the significance of Antarctic ice sheet presence under high-CO_2 scenarios – essential for modelling both past and future climate change[55].

1. Forster, A., Schouten, S., Baas, M. & Sinninghe Damsté, J. S. Mid-Cretaceous (Albian–Santonian) sea surface temperature record of the tropical Atlantic Ocean. *Geology* **35**, 919–922 (2007a).
2. Forster, A. et al. Tropical warming and intermittent cooling during the Cenomanian/Turonian Oceanic Anoxic Event (OAE 2): Sea surface temperature records from the equatorial Atlantic. *Paleoceanography* **22**, PA1219 (2007b).
3. Tarduno, J. A. et al. Evidence for Extreme Climatic Warmth from Late Cretaceous Arctic Vertebrates. *Science* **282**, 2241–2243 (1998).
4. O'Brien, C. L. et al. Cretaceous sea-surface temperature evolution: Constraints from TEX_{86} and planktonic foraminiferal oxygen isotopes. *Earth-Sci. Rev.* **172**, 224–247 (2017).
5. Niezgodzki, I. et al. Late Cretaceous climate simulations with different CO_2 levels and subarctic gateway configurations: A model-data comparison. *Paleoceanography* **32**, 980–998 (2017).
6. Foster, G. L., Royer, D. L. & Lunt, D. J. Future climate forcing potentially without precedent in the last 420 million years. *Nat. Comm.* **8**, doi:10.1038/ncomms14845, (2017).
7. O'Connor, L. K. et al. Late Cretaceous Temperature Evolution of the Southern High Latitudes: A TEX_{86} Perspective. Paleoceanography and Paleoclimatology **34**, doi:10.1029/2018PA003546 (2019).
8. Jenkyns, H. C., Forster, A., Schouten, S. & Sinninghe Damsté, S. High temperatures in the Late Cretaceous Arctic Ocean. *Nature* **432**, 888–892 (2004).
9. Ditchfield, P. W., Marshall, J. D. & Pirrie, D. High latitude palaeotemperature variation: New data from the Tithonian to Eocene of James Ross Island, Antarctica. *Palaeogeogr. Palaeoclimatol. Palaeoecol.* **107**, 79–101 (1994).

10. Bornemann, A. et al. Isotopic Evidence for Glaciation During the Cretaceous Supergreenhouse. *Science* **319**, 189–192 (2008).

11. Müller, R. D. et al. Long-Term Sea-Level Fluctuations Driven by Ocean Basin Dynamics. *Science* **319**, 1357–1362 (2008).

12. Miller, K. G. et al. The Phanerozoic Record of Global Sea-Level Change. *Science* **310**, 1293–1298 (2005).

13. Mcphail, M. K., Truswell, E. M. Palynology of Site 1166, Prydz Bay, East Antarctica. *In: Cooper, A. K., O'Brien, P. E. and Richter, C. (eds.) Proceedings of the Ocean Drilling Program, Scientific Results, College Station, TX (Ocean Drilling Program)* **188**, 1–43 (2004).

14. Mays, C., Steinthorsdottir, M. & Stilwell, J. D. Climatic implications of *Ginkgoites waarrensis* Douglas emend. from the south polar Tupuangi flora, Late Cretaceous (Cenomanian), Chatham Islands. *Palaeogeogr. Palaeoclimatol. Palaeoecol.* **438**, 308–326 (2015).

15. Pujana, R. R., Raffi, M. E. & Olivero, E. B. Conifer fossil woods from the Santa Marta Formation (Upper Cretaceous), Brandy Bay, James Ross Island, Antarctica. *Cretaceous Research* **77**, 28–38 (2017).

16. Manfroi, J. et al. The first report of a Campanian palaeo-wildfire in the West Antarctic Peninsula. *Palaeogeogr. Palaeoclimatol. Palaeoecol.* **418**, 12–18 (2015).

17. Falcon-Lang, H. J., Cantrill, D. J. & Nichols, G. J. Biodiversity and terrestrial ecology of a mid-Cretaceous, high-latitude floodplain, Alexander Island, Antarctica. *J. Geol. Soc. Lond.* **158**, 709–724 (2001).

18. Wang, Y., Huang, C., Sun, B., Quan, C., Wu, J. & Lin, Z. Paleo-CO_2 variation trends and the Cretaceous greenhouse climate. *Earth-Sci. Rev.* **129**, 136–147 (2014).

19. Huber, B. T., MacLeod, K. G., Watkins, D. K. & Coffin, M. F. The rise and fall of the Cretaceous Hot Greenhouse climate. *Glob. Planet. Change* **167**, 1–23 (2018).

20. Arndt, J. E. et al. A new bathymetric compilation covering circum-Antarctic waters. *Geophys. Res. Lett.* **40**, 1–7 (2013).

21. Fretwell, P. et al. Bedmap2: improved ice bed, surface and thickness datasets for Antarctica. *The Cryosphere* **7**, 375–393 (2013).

22. Gohl, K. et al. MeBo70 seabed drilling on a polar continental shelf: operational report and lessons from drilling in the Amundsen Sea Embayment of West Antarctica. *Geochem. Geophys. Geosys.* **18**, 4235–4250 (2017).

23. Lowe, A. L. & Anderson, J. B. Reconstruction of the West Antarctic ice sheet in Pine Island Bay during the Last Glacial Maximum and its subsequent retreat history. *Quat. Sci. Rev.* **21**, 1879–1897 (2002).

24. Spiegel, C. et al. Tectonomorphic evolution of Marie Byrd Land – Implications for Cenozoic rifting activity and onset of West Antarctic glaciation. *Glob. Planet. Change* **145**, 98–115 (2016).

25. Larter, R. D. et al. Reconstruction of changes in the Amundsen Sea and Bellingshausen Sea sector of the West Antarctic Ice Sheet since the Last Glacial Maximum. *Quat. Sci. Rev.* **100**, 55–86 (2014).

26. Gohl, K. et al. Seismic stratigraphic record of the Amundsen Sea Embayment shelf from pre-glacial to recent times: Evidence for a dynamic West Antarctic ice sheet. *Mar. Geol.* **344**, 115–131 (2013).

27. Freudenthal, T. & Wefer, G. Drilling cores on the sea floor with the remote-controlled sea floor drilling rig MeBo. *Geoscientific Instrumentation, Methods and Data Systems* **2**, 329–337 (2013).

28. Crampton, J. S. et al. Cretaceous (Taitai, Clarence, Raukumara and Mata Series). In: Cooper, R.A. (Ed.), The New Zealand Geological Timescale. R. A. Cooper. Lower Hutt, Institute of Geological and Nuclear Sciences Limited. *Geological & Nuclear Sciences Monograph* **22**, 102–122 (2004).

29. Mays, C. & Stilwell, J. D. Pollen and spore biostratigraphy of the mid-Cretaceous Tupuangi Formation, Chatham Islands, New Zealand. *Rev. Palaeobot. Palynol.* **192**, 79–102 (2013).

30. Mildenhall, D. C. Palynological reconnaissance of Early Cretaceous to Holocene sediments, Chatham Islands, New Zealand. *Institute of Geological & Nuclear Sciences monograph* **7** in *New Zealand Geological Survey paleontological bulletin* **67**, 204 p. (1994).

31. He, T., Lamont, B. B. & Fogliani, B. Pre-Gondwanan-breakup origin of Beauprea (Proteaceae) explains its historical presence in New Caledonia and New Zealand, *Science Advances* **2**, E1501648 (2016).

32. Gee, J. & Kent, D. Source of Oceanic Magnetic Anomalies and the Geomagnetic Polarity Timescale. In: Treatise on Geophysics, vol. 5., Geomagnetism, Chapter 5.12, Elsevier, Editor: M. Kono, pp. 455-507, doi:10.1016/B978-044452748-6/00097-3 (2007).

33. Wobbe, F., Gohl, K., Chambord, A. & Sutherland, R. Structure and breakup history of the rifted margin of West Antarctica in relation to Cretaceous separation from Zealandia and Bellingshausen plate motion. *Geochem. Geophys. Geosys.* **13**, 1–19 (2012).

34. Jordan, T. A., Riley, T. R. & Siddoway, C. S. The geological history and evolution of West Antarctica. *Nature Reviews Earth & Environment*, doi:10.1038/s43017-019-0013-6 (2020).

35. Müller, R. D. et al. GPlates: Building a Virtual Earth Through Deep Time. *Geochem. Geophys. Geosys.* **19**, 2243–2261 (2018).

36. DiVenere, V. J., Kent, D. V. & Dalziel, I. W. D. Mid-Cretaceous paleomagnetic results from Marie Byrd Land, West Antarctica: A test of post-100 Ma relative motion between East and West Antarctica, *Journal of Geophysical Research* **99**, B8, 15115–15139 (1994).

37. Pocknall, D. T. & Crosbie, Y. M. Pollen morphology of Beauprea (Proteaceae): Modern and fossil. *Rev Palaeobot and Palynol* **53**, 305–327 (1988).

38. Jackson, M. B. & Armstrong, W. Formation of Aerenchyma and the Processes of Plant Ventilation in Relation to Soil Flooding and Submergence. *Plant Biol* **1**, 274–287 (1999).

39. Lijmbach, G. W. M. On the origin of petroleum. *Proceedings of the 9th world petroleum congress* **2**, 357–369 (1975).

40. Peters, K. E., Walters, C. C. & Moldowan, J. M. The Biomarker Guide. *Cambridge University Press*, 1155 p. (2004).

41. Meyers, P. A. Applications of organic geochemistry to paleolimnological reconstructions: a summary of examples from the Laurentian Great Lakes. *Org. Geochem.* **34**, 261–289 (2003).

42. Robert, C. & Kennett, J. P. Antarctic subtropical humid episode at the Paleocene–Eocene boundary: Clay-mineral evidence. *Geology* **22**, 211–214 (1994).

43. Huang, W. H. & Keller, W. D. Dissolution of rock-forming silicate minerals in organic acids: Simulated first-stage weathering of fresh mineral surfaces. *The American Mineralogist* **55**, 2076–2094 (1970).

44. Sugden, D. E. & Jamieson, S. S. R. The pre-glacial landscape of Antarctica. *Scottish Geographical Journal* **134**, 203–223 (2018).

45. Uenzelmann-Neben, G. & Gohl, K. Early glaciation already during the Early Miocene in the Amundsen Sea, Southern Pacific: Indications from the distribution of sedimentary sequences. *Glob. Planet. Change* **120**, 92–104 (2014).

46. Zundel, M. et al. Thurston Island (West Antarctica) between Gondwana subduction and continental separation: A multistage evolution revealed by apatite thermochronology. *Tectonics* **38**, 878–897 (2019).

47. Müller, R. D., Gohl, K., Cande, S. C., Goncharov, A. & Golynsky, A. V. Eocene to Miocene geometry of the West Antarctic rift system. *Australian Journal of Earth Sciences* **54**, 1033–1045 (2007).

48. Harbert, R. S. & Nixon, K. C. Climate reconstruction analysis using coexistence likelihood estimation (CRACLE): A method for the estimation of climate using vegetation. *American Journal of Botany* **102(8)**, 1277–1289 (2015).
49. Poole, I., Cantrill, D. J. & Utescher, T. Reconstructing Antarctic palaeoclimate from wood floras: a comparison using multivariate anatomical analysis and the Coexistence Approach. *Palaeogeogr. Palaeoclimatol. Palaeoecol.* **222**, 95–121 (2005).
50. Francis, J. E. et al. 100 million years of Antarctic climate evolution: evidence from fossil plants. In: Cooper, A. K. & Barrett, P. et al. (eds.) Antarctica: A Keystone in a Changing World. Proceedings of the 10th International Symposium on Antarctic Earth Sciences. USGS Santa Barbara, California, August 26 to September 1, 2007, The National Academies Press, Washington D.C., USA, pp. 19–27 (2007).
51. Bauersachs, T., Rochelmeier, J. & Schwark, L. Seasonal lake surface water temperature trends reflected by heterocyst glycolipid-based molecular thermometers. *Biogeosciences* **12**, 3741–3751 (2015).
52. Ladant, J. L. & Donnadieu, Y. Paleogeographic regulation of glacial events during the Cretaceous supergreenhouse. *Nat. Comm.* **7**, doi:10.1038/ncomms12771, (2016).
53. Upchurch, G. R. jr., Kiehl, J., Shields, C., Scherer, J. & Scotese, C. Latitudinal temperature gradients and high-latitude temperatures during the latest Cretaceous: Congruence of geologic data and climate models. *Geology* **43**, 683–686 (2015).
54. Farnsworth, A. et al. Climate sensitivity on geological timescales controlled by non-linear feedbacks and ocean circulation. *Geophys. Res. Lett.* **46**, doi:10.1029/2019GL083574 (2019).
55. IPCC. IPCC Special Report on the Ocean and Cryosphere in a Changing Climate. Pörtner, H. O. et al. (eds.), in press. https://www.ipcc.ch/site/assets/uploads/sites/3/2019/12/SROCC_FullReport_FINAL.pdf (2019).

Supplementary Video 1: 3D animation video of the sediment record. Animated video from X-ray computed tomography (CT) data of cores PS104_20-2 9R and 10R.

Acknowledgements

We thank captain and crew of RV *Polarstern* Expedition PS104, as well as the MARUM-*MeBo70* team for their support. The operation of the *MARUM-MeBo70* Sea Floor Drill Rig was funded by the Alfred Wegener Institute (AWI) through its Research Program PACES II Topic 3 and grant no. AWI_PS104_001, the MARUM Center for Marine Environmental Sciences, the British Antarctic Survey through its Polar Science for Planet Earth programme, and the Natural Environmental Research Council funded UK IODP programme. S. Wiebe, R. Fröhlking, V. Schumacher, N. Lensch, M. Arevalo, M. Seebeck, and H. Grobe are thanked for their help on board and in the lab, respectively. The *Klinikum Bremen-Mitte* (A.-J. Lemke and C. Tiemann, *Gesundheit Nord* Bremen) is acknowledged for providing facilities for computed core tomographies, and M. Köhler (MKfactory, Germany) for preparing the thin sections. J. McKay (University of Leeds) is thanked for creating and painting the Late Cretaceous West Antarctic palaeoenvironment based on reconstructions presented here. J.P.K, G.K., K.G., J.M. G.U.-N., O.E., C.G., T.R. and R.D. were funded by the AWI PACES II programme. J.P.K. and J.M. were additionally funded through the Helmholtz Association (PD-201 & VH-NG-1101). UK IODP funded participation of T.v.d.F., P.S.P. and S.M.B. in expedition PS104. J.T. was funded through the Cluster of Excellence "The Ocean Floor – Earth's Uncharted Interface" at the University of Bremen.

Author contributions

J.P.K. led the study and together with U.S., T.B., C.-D.H., K.G. and G.K., conceived the idea for the study and wrote the manuscript. J.P.K, T.B., C.-D.H., S.B., J.A.S., K.G., T.F, T.v.d.F., P.S.P., W.E., O.E., H.P. and T.R. collected the cores. J.P.K, C.-D.H., T.B. and G.K. undertook the sedimentological and U.S. and S.B. the palynological analyses. T.B. and G.K. conducted the XRF scanning and processing of the cores. G.K. carried out the grain-size and bulk mineralogical analyses. J.T. led the CT scanning, processing, and visualization. J.M. performed the biomarker analyses together with Th.B. (heterocyst glycolipid palaeothermometry). T.F. conducted the palaeomagnetic measurements. J.E.F., G.N., G.K. and J.P.K. investigated the thin sections. W.E. analysed the clay mineral assemblages and T.v.d.F. and P.S.P. measured bulk sediment Nd and Sr isotope compositions. K.G., R.D.L., and T.F. helped determining the palaeolatitude of the drill site. G.L. and I.N. undertook the modelling with COSMOS. M.Z., C.S., C.M. and D.C. provided the U/Pb age constraints. U.S. and F.S. performed the bioclimatic analyses. J.P.K., T.B., C.-D.H., S.B., T.F., W.E., J.A.S., O.E., O.E., H.P., T.R. and R.D. helped sampling and scanning the cores. K.G., G.U.-N. and R.D.L. undertook the seismic pre-site survey. All members of the Expedition PS104 Science Team helped in pre-site survey investigations, core recovery, on-board analyses and/or shore-based measurements. K.G., G.K., C.-D.H., G.U.-N., T.B. and R.D.L. acquired funding, proposed, and planned RV *Polarstern* expedition PS104. All co-authors commented on the manuscript and provided input to its final version.

Author information

Reprints and permissions information is available at www.nature.com/reprints. The authors declare no competing financial interests. Readers are welcome to comment on the online version of the paper. Correspondence and requests for materials should be addressed to J.P.K. (Johann.Klages@awi.de).

Science Team of Expedition PS104

Afanasyeva, V., VNIIOkeangeologie, St. Petersburg, Russia

Arndt, J. E., Alfred-Wegener-Institut, Helmholtz-Zentrum für Polar- und Meeresforschung, Bremerhaven, Germany

Ebermann, B., Technische Universität Dresden, Dresden, Germany

Gebhardt, C., Alfred-Wegener-Institut, Helmholtz-Zentrum für Polar- und Meeresforschung, Bremerhaven, Germany

Hochmuth, K., Alfred-Wegener-Institut, Helmholtz-Zentrum für Polar- und Meeresforschung, Bremerhaven, Germany, now at: School of Geology, Geography and the Environment, University of Leicester, Leicester, UK

Küssner, K., Alfred-Wegener-Institut, Helmholtz-Zentrum für Polar- und Meeresforschung, Bremerhaven, Germany

Najman, Y., Lancaster Environment Centre, Lancaster University, Lancaster, UK

Riefstahl, F., Alfred-Wegener-Institut, Helmholtz-Zentrum für Polar- und Meeresforschung, Bremerhaven, Germany

Scheinert, M., Technische Universität Dresden, Dresden, Germany

Figure captions

Figure 1: Setting of *MARUM-MeBo70* drill site PS104_20-2 on the Amundsen Sea Embayment (ASE) shelf. a) The modern configuration of West Antarctica is placed in relation to the reconstructed boundary between continental and oceanic crust (COB) at 84 Myr[33,34] (thick black lines). The pre-break up suture (dashed white line) indicates the position of the reconstructed Zealandian and West Antarctic COBs prior to initial break-up starting at ~90 Myr[33]. Orange circles mark the locations of other outcrops of mid-Cretaceous sedimentary strata[13–17]. b) Seismic reflection profile NBP9902-11[23] (A-B) crossing drill site 20-2: orange bar indicates drilled core length. The profile position is indicated in “a”. The drill hole penetrated Amundsen Sea shelf unconformity ASS-u1, which separates seismic units ASS-1 and ASS-2[26]. Interpretation of seismostratigraphic units and unconformities is based on both previous work[26] and this study. Pitt Island belongs to the Chatham Island group of New Zealand. PB: Prydz Bay; ChR: Chatham Rise. Shelf bathymetry and sub-ice topography data derive from refs. 20 and 21.

Figure 2: Multi-proxy parameter reconstruction of cores 9R and 10R at site PS104_20-2. The *MARUM-MeBo70* sea floor drill rig drilled 30.7 m into the seafloor and recovered 5.91 m of core length. The lower ~3 m consist of a fossil root-bearing mudstone with a ~5 cm-thin layer

of brecciated lignite on top (from ~26.77 mbsf downwards) both of Turonian–Santonian age. A Late Eocene or younger quartzitic sandstone overlies the lignite. The upper lignite boundary defines the impedance contrast between the underlying mudstone and overlying quartzitic sandstone and likely coincides with the prominent regional unconformity ASS-u1[26] (see thick red line in Fig. 1b). Note the core break between 9R and 10R at 27.15 mbsf. (LS: Linescan; CT: X-Ray computed tomography; Cl/St/Sd: Clay/Silt/Sand; TOC: Total organic carbon; Gy/An/Pt/Br: Gymnosperms/Angiosperms/Pteridophytes/Bryophytes; x: Barren palynomorph samples; Fe(Ca): Iron-carbonate; Bulk sediment neodymium (ε_{Nd}) values (±2 S.D. = 0.27) and strontium ($^{87}Sr/^{86}Sr$) ratios (±2 S.E. = see Source data) (see Methods); TAR: Ratio of terrestrial and aquatic-sourced *n*-alkanes; C:N (mol.): molar ratio of total organic carbon (TOC) to total nitrogen (TN); *: Zircon U-Pb age (45.5 Myr); mbsf: meters below sea floor). Inferred ages are based on palynomorph biostratigraphy for the mudstone and U/Pb ages of apatite and zircon grains for the sandstone (see text). Data link to PANGAEA (DOI in progress): https://doi.pangaea.de/10.1594/PANGAEA.906092.

Figure 3: Modern and mid-Cretaceous CO_2 sensitivity runs. Distribution of warmest mean month temperatures (WMMT) (°C) for present (upper row: a-c) and mid-Cretaceous at 90 Myr (lower row: d-f) configurations for atmospheric CO_2 levels of 280, 560, 1120 ppm, representing 1x, 2x and 4x pre-industrial CO_2 level of 280 ppm. The black triangle indicates the approximate position of site PS104_20-2 (a–c: modern; d–f: Turonian–Santonian). g) Modelled mid-Cretaceous WMMT (dashed coloured lines) and zonal mean temperatures (full coloured lines) for different atmospheric CO_2 concentrations. The temperature estimates, including their respective calibration error (2σ), were derived from the following proxies referred to in ref. 5: terrestrial $\delta^{18}O$ of vertebrate tooth enamel and/or pedogenic carbonate (full squares), palaeobotanical data (full circles), fish enamel $\delta^{18}O$ (open triangles), marine calcareous fossil $\delta^{18}O$ (open diamonds), and biomarkers (cross). Temperature estimates from this study are indicated as a red full circle and cross, respectively.

Figure 4: Visual reconstruction of the West Antarctic Turonian–Santonian temperate rainforest. The painting is based on palaeo-floral and environmental information inferred from palynological, geochemical, sedimentological, and organic biomarker data obtained from cores 9R and 10R at site PS104_20-2. The creation of the painting was further complemented by published palaeo–topographic and palaeo–tectonic information[24,26,33,34]. Original size of painting: 83.8 x 41.5 cm. Alfred-Wegener-Institut/J. McKay; this image is available under Creative Commons licence CC-BY 4.0.

Methods

Sea Floor Drill Rig *MARUM-MeBo70*

The sea floor drill rig *MARUM-MeBo70* is a robotic drill rig that was deployed on the seabed and remotely controlled from RV *Polarstern* during expedition PS104[22]. Detailed information about the drill rig and its operation is published in ref. 27.

X-ray computed tomography

Whole rounds of *MeBo* core PS104_20-2 were scanned by a *Toshiba Aquilion 64*™ computer tomograph (CT) at the hospital *Klinikum Bremen-Mitte*, with an X-ray source voltage of 120 kV and a current of 600 mA. The CT scans have a resolution of 0.351 mm in x- and y-direction and 0.5 mm resolution in z-direction (resolution of scaled reconstruction: 0.195 x 0.195 x 0.3 mm). Images were reconstructed using Toshiba's patented helical cone beam reconstruction technique. The obtained CT data were processed using the ZIB edition of the *Amira* software (version 2017.39)[56]. Within *Amira*, the CT scans of the core sections were merged when necessary and core liners, including about 2 mm of the core rims, were removed from the dataset until all marginal artefacts from the coring process were removed. Subsequently, all clasts > ~1 mm, root-traces (where present) and matrix sediment were segmented with the (marker-based) watershed tool of the *Segmentation Editor*. Markers were predominantly set by density thresholding. Holes within clasts after the watershed segmentation were added to the clasts with the *selection fill* tool. Only in exceptional cases, markers were segmented by hand.

Palynology

Between 2 and 6 g of dry weight sediment per sample were processed at Northumbria University, following standard palynological techniques, including sieving (10 μm) and acid treatment with 10% HCl (Hydrochloric acid) and cold 38% HF (Hydrofluoric acid). The processed residue was transferred to microscope slides using glycerine jelly as a mounting medium, and 2–3 slides were analysed per sample at 400x magnification. Of the 17 samples analysed for pollen and spores, 7 were productive, and total counts range from 340 to 360 pollen and spores per sample (Extended Data Figs. 2, 3; Extended Data Table 1). Pollen concentrations increase from an average of ~6,500 grains/g sediment in the lower three samples to 61,000–121,500 grains/g at the top. We could not identify any reworking of palynomorphs. Percentages were calculated based on the sum of total pollen and spores. 65 pollen and spore taxa were identified from the literature[57–59] (Extended Data Table 3). All samples contained a high morphological diversity of *Podocarpus* pollen, which we classified as *Podocarpidites* undiff., as many of these grains were either folded or damaged and were therefore unidentifiable beyond family level. Marine dinoflagellate cysts were absent in all samples.

Palynomorph-based climate reconstructions (Bioclimatic analysis)

We reconstructed terrestrial mean annual temperature (MAT), precipitation (MAP) and mean warmest month temperature (WMMT) using the Nearest Living Relative (NLR) approach. The NRL approach uses the climatic requirements of the NLR of fossil taxa to reconstruct the past climatic range and assumes that the climatic requirements of the fossil taxa are similar to those of their NLR (Extended Data Table 2). NLR approaches use the presence or absence of individual taxa in fossil assemblage rather than relative abundance, which reduces the likelihood of taphonomic biases. This facilitates, to some extent, the reconstruction of past non-modern analogue climates and environments[60]. NLR-based temperature estimates are generally in good agreement with estimates from geochemical and other palaeobotanical methods, including the Climate Leaf Analysis Multivariate Program (CLAMP) and Leaf Margin Analysis[61–67] providing confidence in the utility of the method for the reconstruction of “deep-time” climates.

However, quantitative climate estimates from the fossil plant record of “deep-time” geological intervals are always accompanied by large uncertainties. Incorrect use of outliers and fossil taxa with ambiguous affinity can result in erroneous climate estimates[68]. One of the greatest weaknesses that affects all NLR approaches is the assumption of uniformitarianism, namely that the climate tolerances of modern species can be extended into the past. This assumption inevitably introduces uncertainty that increases with the age of the geological formation[69]. In order to statistically constrain the most likely climatic co-occurrence envelope, we combined the NLR approach with the probability density function (PDF) method[70–72]. In contrast to other NLR methods, such as the Coexistence Approach, the PDF method has the advantage that it statistically constrains the most likely climatic co-occurrence envelope, thereby offering a solution to mathematically reduce the potential impact of wrongly defined climate tolerance on upper and lower limits of palaeoclimatic estimates. In order to further reduce uncertainties caused by potentially wrong identification of NLR, we removed fossil taxa with potentially ambiguous affinity or very rare occurrence in the fossil record (Extended Data Table 2). This includes *Microcachryidites antarcticus*, a taxon abundant and widespread in the fossil Antarctic record, with the NLR *Microcachrys tetragona*, the sole species of the genus Microcachrys, that nowadays is endemic to Tasmania. Another example is *Peninsulapollis gillii* with close links to the modern genus *Beauprea*, and endemic to New Caledonia. In both cases we used the family, Podocarpaceae and Proteaceae, respectively, rather than the genus or species as the NLR.

To generate the paleoclimate estimate, we followed the procedure described in refs. 59 and 63. We first identified the bioclimatic envelope for each NLR by cross-plotting their modern distribution from the Global Biodiversity Information Facility (GBIF)[73] with the gridded

WorldCLIM climate surface[74] using the “dismo” package[75] in R. We then filtered the dataset and removed redundant data, “exotic” occurrences (such as garden plants) as well as multiple entries per climate grid cell to avoid the climatic probability function becoming highly slanted towards that location[76]. Before establishing the probability density functions, bootstrapping was applied to test the robustness of the dataset, which is of particular interest for taxa with only few modern occurrences. Following the bootstrapping, we calculated the likelihood (f) of a taxon (t) occurring at value (x) for a certain climatic variable by using the mean (μ) and standard deviation (σ) of the modern distribution range of each taxa[65,70].

$$f(x)_t = \frac{1}{\sqrt{2\pi\sigma_x^2}}\, e^{-\frac{(x-\mu_x)^2}{2\sigma_x^2}}$$

Since the separate reconstruction of climate ranges for each variable can lead to bioclimatic envelopes that include intervals, where no modern-day occurrence of taxon t is observed[65], we calculated joint likelihood PDFs for each combination of climate variables MAT, MAP and WMMT using the correlation coefficient p (x, y):

$$f(x,y)_t = \frac{1}{2\pi\sigma_x\sigma_y\sqrt{1-p^2}}\, e^{-\frac{1}{2(1-p^2)}\left(\frac{(x-\mu_x)^2}{2\sigma_x^2}+\frac{(y-\mu_y)^2}{2\sigma_y^2}-2p\frac{(x-\mu_x)(y-\mu_y)}{\sigma_x\sigma_y}\right)}$$

After assessing if all bioclimatic envelopes share a coexistence interval, the climate estimates of the NLR assemblage were reconstructed by multiplying the individual joint likelihoods of taxa $f(x, y)_{t1}$… $f(x, y)_{tn}$ with each other:

$$f(x,y)_{Combined} = f(x,y)_{t1}\ x\ f(x,y)_{t2}\ x \dots x\ f(x,y)_{tn}$$

In order to constrain the core distribution of a group, we determined the range of one ($f(x, y)_{relative}$ = 0.157) and two standard deviations ($f(x, y)_{relative}$ = 0.023) from the occurrence within a group with $f(x, y)_{max}$ representing the most likely climate conditions[76].

$$f(x,y)_{relative} = \frac{f(x,y)}{f(x,y)_{max}}$$

For our bioclimatic analysis we used all pollen and spore taxa that could be related to an NLR, following ref. 59 (Extended Data Table 2). Climatic ranges are indicated with their ±2 σ range. For our record we calculated mean annual temperatures of 12.8±2.2°C, warmest mean month temperatures of 18.4±1.9°C, and mean annual precipitation of 1,120±330 mm/a. It should be noted that the ranges of these values show the mathematical error and not the real range, which might result from the uncertainties of using an NRL approach method. To avoid misunderstandings, we therefore indicated in the main text the pollen-based climate estimates without 2 σ ranges.

Organic geochemistry

Freeze-dried and homogenized sediment samples were extracted by means of ultrasonication using a dichloromethane:methanol mixture (2:1, v:v). After centrifugation, the total lipid extract was dried by rotary evaporation. The extraction was repeated twice. The combined total lipid extract was fractionated using silica open-column chromatography and hexane as eluent to obtain apolar lipids. Hydrocarbons were analysed using an HP gas chromatograph 6890 (30 m DB-5MS column, 0.25 mm diameter, 0.25 µm film thickness). The identification of *n*-alkanes, pristane, and phytane was based on comparison of their retention times with those of reference compounds that were run on the same instrument. The terrigenous-aquatic-ratio (TAR[77] was calculated using peak areas of long-chain (n-C_{27}, n-C_{29}, n-C_{31}) against short-chain (n-C_{15}, n-C_{17}, n-C_{19}) alkanes. The carbon preference index (CPI) was calculated as follows[40]:

(1) $CPI = 2*(n\text{-}C_{23}+n\text{-}C_{25}+n\text{-}C_{27}+n\text{-}C_{29})/(n\text{-}C_{22}+2*(n\text{-}C_{24}+n\text{-}C_{26}+n\text{-}C_{28})+n\text{-}C_{30})$.

Heterocyst glycolipid palaeothermometry

Sediment samples from the coastal sandstone (9R, 50-52 cm; 2676 cmbsf) and the carbonaceous mudstone (9R, 76.5–78 cm; 27.02 mbsf; 10R, 60–62 cm; 29.21 mbsf) were lyophilized and ground to fine sediment powder using a solvent-cleaned agate pestle and mortar. Between 20.1 and 29.7 g of sediment was extracted using a modified Bligh and Dyer procedure[78]. Briefly, the cell material was extracted ultrasonically thrice for 10 min each in a solvent mixture of MeOH, DCM and phosphate buffer (2:1:0.8; v:v:v). After each sonication step, the solvent mixture was centrifuged at 1,500 x g for 3 min and the supernatant transferred to a centrifuge tube. The combined supernatants were phase separated by adding DCM and phosphate buffer to a final solvent ratio of 1:1:0.9 (v:v:v). The organic bottom layer was collected in a round bottom flask and reduced under vacuum using a rotary evaporator. Each Bligh and Dyer extract (BDE) was transferred to a pre-weighed vial using DCM:MeOH (1:1, v:v) and dried under a gentle stream of N_2. Prior to analysis, all BDEs were re-dissolved in a solvent mixture of *n*-hexane:2-propanol:H_2O (72:27:1; v:v:v) to a concentration of 8 mg/ml. In order to test for possible cross contamination during sample preparation a blank was included in each batch and treated as a regular sample.

High performance liquid chromatograph coupled to electrospray ionisation tandem mass spectrometry (HPLC/ESI-MS^2) was performed on the BDEs following the analytical procedure given by ref. 79 to establish heterocyst glycolipid (HG) distribution patterns and relative abundances. Separation of HGs was achieved using a Waters Alliance 2690 HPLC system fitted with a Phenomenex Luna NH_2 column (150 x 2 mm; 3 μm particle size) and a guard column of the same material. Both were maintained at a constant temperature of 30°C. The applied gradient profile was as follows: 95% A/5% B to 85% A/15% B in 10 min. (isocratic for 7 min) at 0.5 ml min^{-1}, followed by back flushing with 30 % A/70% B at 0.2 ml min^{-1} for 25 min. and re-equilibrating the column with 95% A/5% B for 15 min. Solvent A was *n*-hexane:2-propanol:HCO_2H:14.8 M NH_3 aq. (79:20:0.12:0.04; v:v:v:v) and Solvent B was 2-propanol:water:HCO_2H:14.8 M NH_3 aq. (88:10:0.12:0.04; v:v:v:v).

Heterocyst glycolipids were detected using a Micromass Quattro LC triple quadruple mass spectrometer equipped with an electrospray ionisation (ESI) interface and operated in

positive ion mode. Source conditions were as given in ref. 80. All BDEs were analysed in multiple reaction monitoring (MRM) mode to achieve maximum specificity and HGs identified based on comparison of retention times with those of HGs in cultured cyanobacteria as well as published mass spectral information[81–85]. HGs were monitored using the following transitions: *m/z* 547 → 415 (pentose HG_{26} diol), *m/z* 603 → 471 (pentose HG_{30} diol), *m/z* 619 → 487 (pentose HG_{30} triol), *m/z* 647 → 515 (pentose HG_{32} triol), *m/z* 561 → 415 (deoxyhexose HG_{26} diol), *m/z* 575 → 413 (HG_{26} keto-ol), *m/z* 577 → 415 (HG_{26} diol), *m/z* 603 → 441 (HG_{28} keto-ol), *m/z* 605 → 443 (HG_{28} diol), *m/z* 619 → 457 (HG_{28} keto-diol), *m/z* 621 → 459 (HG_{28} triol), *m/z* 635 → 459 (methylated hexose HG_{28} triol), *m/z* 647 → 485 (HG_{30} keto-diol), *m/z* 649 → 487 (HG_{30} triol), *m/z* 675 → 513 (HG_{32} keto-diol), *m/z* 677 → 515 (HG_{32} triol) and quantified by integrating peak areas using the QuanLynx application software.
Surface water temperatures (SWTs) during the deposition of the coastal Eocene sandstone were re-constructed using the HDI_{26} (heterocyst diol index of 26 carbon atoms) and HDI_{28} (heterocyst diol index of 28 carbon atoms) lipid palaeothermometers as described by ref. 51. As the HG content of the swampy palaeoenvironment exclusively consisted of HG_{30} triols and HG_{30} keto-diol (Extended Data Fig. 4), which are specific for cyanobacteria forming benthic microbial mats[83], we here applied the HTI_{30} (heterocyst triol index of 30 carbon atoms) to the mudstone sequence. This index is defined as follows:

$$HTI_{30} = HG_{30}\ \text{triol} / (HG_{30}\ \text{triol} + HG_{30}\ \text{keto-diol})$$

The HTI_{30} was transferred to absolute temperatures using a surface sediment calibration obtained from a large set of East African lakes (n = 47) located on an altitudinal transect from 615 to 4504 masl and SWTs ranging from 5.7 to 27.9°C. In this setting, the HTI_{30} showed a strong linear correlation with SWT, which is expressed in the equation below (Bauersachs, unpublished data):

$$SWT = (HTI_{30} / 0.0249) – (0.2609 / 0.0249)$$

Independent conformation for the robustness of the HG-based temperature reconstruction is obtained by comparing HG distribution patterns and HTI_{30} values in the mudstone sequence with those reported for an axenic culture of the heterocystous cyanobacterium *Scytonema* sp. PCC 10023 (ref. 85). This cyanobacterium exclusively contains HG_{30} triols and HG_{30} keto-diols. The above transfer function predicts a HTI_{30} of ~0.88 for the culture grown at an ambient temperature of 25°C, which is in the same order of magnitude as the HTI_{30} calculated using the relative abundances of the major HG_{30} triol and HG_{30} keto-diol isomers reported in ref. 85.

Grain-size analyses

A set of discrete samples was wet sieved at 2 mm and 63 μm to separate the grain-size classes gravel, sand, and mud. The < 63 μm (mud) suspension was separated into silt (2 to 63 μm) and clay (< 2 μm) using settling velocity (Stokes' Law) in Atterberg tubes.

Clay mineral analyses

An aliquot of the clay fraction was used to determine the relative contents of the clay minerals smectite, illite, chlorite, and kaolinite using an automated powder diffractometer system Rigaku MiniFlex with CoKα radiation (30 kV, 15 mA) at the Institute for Geophysics and Geology (University of Leipzig). The clay mineral identification and quantification followed standard X-ray diffraction methods[86].

Bulk sediment composition

Total carbon (TC) and total nitrogen (TN) were analysed with an Elementar Vario EL III. Total organic carbon (TOC) contents were determined after removal of the total inorganic carbon (TIC, carbonates) with HCl using an ELTRA CS-2000. Carbonate content was calculated by subtracting the TOC from the TC and multiplying the difference (TIC) by 8.33, i.e. the ratio between the molecular weights of $CaCO_3$ and C. The TOC:TN (C:N) ratio was calculated on a molar basis.

The mineralogical composition of the milled bulk sediment was analysed semi-quantitatively with X-ray diffraction using peak intensities and area ratios analysed with the MacDiff program[87]. For the Fe(Ca)-carbonates the peak intensities for ankerite (at 2.9 Å) and siderite (at 2.791 Å) were used and summed up as percentages for Fe(Ca)-carbonates (ankerite and siderite) in relation to the absolute % of other carbonates (calcite, Mg-calcite, and dolomite).

Thin sections

After drying the untreated soft sediment in the fridge for 2–3 days, the sediment was dried at room temperature (20–22°C) for another 2–3 days. During that time the sediment was checked daily for crack formation. Under low pressure, the sediment was impregnated stepwise in a vacuum exicator with epoxy araldite 2020 resin until full coverage of the sample. After complete hardening, the bottom of the sample was ground by a Tegrapol with silicon carbid (SiC) paper sizes from 80 to 800 – depending on sediment characteristics – and a maximum of 150 rotations per minute until reaching the sediment surface. The glasses for covering the thin sections with a thickness of 3 mm and a diameter of 35x120 mm were ground with a 9-micron fraction SiC paper to achieve both grip and an even surface (alternative machine system: Logitech LP50 auto). Then the sample was attached to the glass with the same resin used for impregnation by a pressure block. Afterwards, the surface of the glass was cleaned and labelled with a diamond pen. Most samples were then cut by a WOCO 50 diamond saw for achieving 250 µm-thick sediment stripes on the glass, before grounding with SiC paper or the Logitech LP50 to reach a thickness of 30 µm. Some sections were covered with 150 µm-thick glasses, for which an ultraviolet resin (cyanacrylate) was used. Most sections remained uncovered for Raman and SEM-EDX spectroscopy. Finally, all thin sections were cleaned with ethanol. The set of thin sections was prepared by MKfactory (Stahnsdorf, Germany).

Palaeomagnetic measurements

Five discrete samples were taken with variable spacing from cores 9R and 10R of core PS104_20-2 for palaeomagnetic investigations using plastic boxes with inner dimensions of 2×2×2 cm. Directions and intensities of natural remanent magnetization (NRM) were measured on a cryogenic magnetometer (model 2G Enterprises 755 HR). Subsequent alternating field demagnetization of NRM involved 15 steps to a maximum AF intensity of 100 mT. A detailed vector analysis[88] was applied to the results in order to determine the characteristic remanent magnetization (ChRM) of each sample and to unravel its magnetic polarity. Samples showing no systematic demagnetization pattern were excluded from further interpretation.

Palaeoclimate modelling

We use the COSMOS model (see Code availability) in a coupled atmosphere-ocean configuration with fixed vegetation. The atmosphere component ECHAM5 is run in a T31/L19 resolution[89]. It consists of 19 vertical layers and has a horizontal resolution of ~3.75°. The ocean component MPI-OM runs in GR30/L40 configuration[90]. It has a formal horizontal resolution of 3.0° x 1.8° and consists of 40 unequal vertical layers. The high-resolution hydrological discharge model is a part of ECHAM5[91] while MPI-OM includes a dynamic-thermodynamic sea-ice model utilizing a viscous-plastic rheology[92]. Climate simulations were run for present and mid-Cretaceous configurations under different CO_2 levels in the atmosphere. Other greenhouse gases (such as CH_4 and N_2O) were set to pre-industrial (PI) level. In the mid-Cretaceous simulations, we employ published paleogeography[93] and vegetation[94] as well as no ice sheets on both hemispheres. The orbital configurations in all Cretaceous experiments were fixed at 800 common era (CE) and hence represent values from the beginning of externally forced simulation from 800 to 1,800 CE (so called millennial run). The solar constant was reduced by 1% for the mid-Cretaceous experiments relative to the present-day value. The simulations with 1x and 2x PI CO_2 levels were run for 9,200 and 9,000 years, respectively, while 10,600 years for 4x PI CO_2 (ref. 95). All simulations reached equilibrium at the surface. The experiment with 6x PI CO_2 level had a slightly different atmospheric land-sea mask than the other three simulations. It was run for ~500 years and was not in a full equilibrium at the surface[5]. The pre-industrial control simulation was run for ~7,500 years. The simulations with 2x and 4x PI CO_2 levels were branched off from 1x PI simulation from the year 6,800 and were further run for 700 years. The simulations reach either full or quasi equilibrium at the surface. For the analyses the mean was taken over the last 100 years of each simulation. The model has been successfully applied previously for scientific questions focusing on the Quaternary[96,97], Neogene[98–100]; Palaeogene[101,102], Late Cretaceous[5] as well as estimates of future climate[100,103].

Sr and Nd isotopic measurements

A total of seven samples were selected for processing from cores 9R and 10R at site PS104_20-2. A detailed method description that was applied for determining their Sr and Nd isotopic compositions is given in ref. 104.

Zircon and apatite U-Pb geochronology

The youngest detrital zircon and apatite U-Pb ages obtained from the cores 2R (sample AWI-35 at 9.9 mbsf) and 9R (sample AWI-25 at 26.7 mbsf) were used for constraining maximum deposition ages of the sandstone. The samples yielded Eocene apatite (n=2) and zircon (n=1) ages. The single Eocene zircon grain yields a Concordia age of 45.5±2.0 Myr (Extended Data Fig. 1a). The apatite grains all yield analyses discordant in U-Pb isotopic space due to the presence of common-Pb (Pb_c; i.e. Pb incorporated during crystallisation as opposed to radiogenic Pb* generated *in-situ* by radionuclide decay). For single-grain ages a terrestrial Pb-isotope evolution model[105] was used for an initial estimate of $^{207}Pb_c/^{206}Pb_c$, followed by an iterative approach to the ^{207}Pb-based corrected age calculation[106].
As only two Eocene single-grain apatite ages are reported, calculation of an array age would not normally be indicated. However, comparison of the trace element chemistry (REE-Sr-Y) to an apatite compositional reference library[107] indicates both Eocene grains are chemically as well as chronologically indistinguishable (Extended Data Fig. 1b), increasing the likelihood

of a common source. Therefore, the two youngest apatite grains from AWI-35 were jointly regressed with the range of $^{207}Pb_c/^{206}Pb_c$ values (0.834 ± 0.018) for West Antarctic crystalline basement[108] (Extended Data Fig. 1a) to obtain a lower-intercept age of 39.3±3.8 Myr (MSWD = 0.99), similar to the independently-obtained single-grain Concordia age of 45.5±2.0 Myr yielded by the youngest zircon from AWI-25. A Lutetian maximum deposition age (ca. 43 Myr) for AWI-35 and AWI-25 is therefore indicated.

Pure apatite and zircon separates were handpicked from the non-magnetic heavy mineral 63-315 μm size fraction, mounted in epoxy resin, ground to reveal internal surfaces, and polished. Virtually no sample bias was introduced by grain selection because in most cases all observed mineral grains were picked as the amount of sample material was very small. All U-Pb analyses were carried out using a Photon Machines Analyte Excite 193 nm ArF excimer laser-ablation system with a HelEx 2-volume ablation cell coupled to an Agilent 7900 ICPMS at the Department of Geology, Trinity College Dublin, Ireland. Laser fluence was 2.5 J cm^{-2} with a repetition rate of 15 Hz and analysis time of 20 s, followed by an 8 s pause to allow for signal washout and a subsequent baseline measurement. Spot sizes of 47 μm and 24 μm were employed for apatite and zircon respectively, in separate analytical sessions.

Data reduction employed the Vizual_Age and VisualAge_UComPbine data reduction schemes (DRS) for Iolite for zircon and apatite, respectively[109–111]. Each DRS corrects for intra-session analytical drift, mass bias, and downhole fractionation using a user-specified fractionation model based on measurements of the primary standard; additionally, VisualAge_UComPbine permits the presence of a variable Pb_c content in a primary age standard to be corrected for using a known initial $^{207}Pb_c/^{206}Pb_c$ value. Final U-Pb age calculations were made using the Isoplot add-in for Excel[112].

Single-grain zircon U-Pb Concordia ages were calculated, and analyses with probability of concordance <0.001 were rejected[112]. The primary standard was Plešovice zircon; the GZ7 and 91,500 zircons were utilised as secondary standards and treated as unknowns during data reduction and age calculation[113], yielding Concordia ages of 530.1±3.7 Myr and 1060.4±6.8 Myr, respectively.

For apatite analyses, Madagascar apatite was employed as the primary standard and McClure Mountain and Durango apatites were employed as secondary standards[114,115]. Pb_c in the secondary standards was corrected for using fixed initial ratios, yielding weighted mean ages of 532.2±6.0 Myr and 32.3±0.7 Myr, respectively. Variable common Pb contents in the detrital apatite unknowns were corrected by using a terrestrial Pb evolution model[104] for calculation of single-grain ages followed by an iterative calculation to obtain single-analysis ^{207}Pb-corrected ages[105]. Alternatively, the range of $^{207}Pb_c/^{206}Pb_c$ values for West Antarctic basement[106] can be used for the single-grain age calculation: the resulting single-grain ages are within 1 Myr of the single-grain ages obtained using the iterative calculation. Apatite U-Pb age filtering[116] permitted grains with ages of 10–100 Myr to have 2σ errors ≤50% and grains with ages >100 Myr to have 2σ errors ≤25%. For apatite trace-element analysis, the Iolite Trace Elements DRS was utilised. NIST612 glass and Madagascar apatite[117] were employed as the primary and secondary reference materials respectively, with ^{43}Ca as an internal elemental standard[118].

56. Stalling, D., Westerhoff, M. & Hege, H.-C. Amira: A Highly Interactive System for Visual Data Analysis. *In: Hansen, C. D. and Johnson, C. R. (eds.) The Visualization Handbook, Elsevier, The Netherlands*, 749–767 (2005).
57. Raine, J.I., Mildenhall, D.C. & Kennedy, E.M. New Zealand fossil spores and pollen: an illustrated catalogue. 4th edition. *GNS Science miscellaneous series* **4**, http://data.gns.cri.nz/sporepollen/index.htm" (2011).
58. Mays, C. A late Cretaceous (Cenomanian-Turonian) south polar palynoflora from the Chatham Islands, New Zealand. *Memoirs of the Association of Australasian Palaeontologists* **47**, 92 pp (2015).
59. Bowman, V. C., Francis, J. E., Askin, R. A., Riding, J. B. & Swindles, G. T. Latest Cretaceous-earliest Paleogene vegetation and climate change at the high southern

latitudes: palynological evidence from Seymour Island, Antarctic Peninsula. *Palaeogeogr. Palaeoclimatol. Palaeoecol.* **408**, 26–47 (2014).

60. Utescher, T. et al. The Coexistence Approach—Theoretical background and practical considerations of using plant fossils for climate quantification. *Palaeogeogr. Palaeoclimatol. Palaeoecol.* **410**, 58–73 (2014).

61. Ballantyne, A.P., Greenwood, D.R., Sinninghe Damsté, J.S., Csank, A.Z., Eberle, J.J. & Rybczynski, N. Significantly warmer Arctic surface temperatures during the Pliocene indicated by multiple independent proxies. *Geology* **38**, 603–606 (2010).

62. Uhl, D., Mosbrugger, V., Bruch, A. & Utescher, T. Reconstructing palaeotemperatures using leaf floras-case studies for a comparison of leaf margin analysis and the coexistence approach. *Rev Palaeobot and Palynol* **126**, 49–64 (2003).

63. Pound, M.J. & Salzmann, U. Heterogeneity in global vegetation and terrestrial climate change during the late Eocene to early Oligocene transition. *Scientific Reports* **7**, 43386 (2017).

64. Pross, J. et al. Persistent near-tropical warmth on the Antarctic continent during the early Eocene epoch. *Nature* **488**, 73–77 (2012).

65. Willard, D. A. et al. Arctic vegetation, temperature, and hydrology during Early Eocene transient global warming events. *Global and Planetary Change* **178**, 139–152 (2019).

66. Kennedy, E.M. Late Cretaceous and Paleocene terrestrial climates of New Zealand: leaf fossil evidence from South Island assemblages. *N. Z. J. Geol. Geophys.* ***46,*** 295–306 (2003).

67. Kennedy, E.M., Arens, N.C., Reichgelt, T., Spicer, R.A., Spicer, T.E.V., Stranks, L., Yang, J. Deriving temperature estimates from southern hemisphere leaves. *Palaeogeogr. Palaeoclimatol. Palaeoecol.* **412**, 80–90 (2014).

68. Grimm, G. W., Bouchal, J. M., Denk, T. & Potts, A. Fables and foibles: A critical analysis of the Palaeoflora database and the Coexistence Approach for palaeoclimate reconstruction. *Rev. Palaeobot. Palynol.* **233**, 216–235 (2016).

69. Hollis, C. J. et al. The DeepMIP contribution to PMIP4: methodologies for selection, compilation and analysis of latest Paleocene and early Eocene climate proxy data, incorporating version 0.1 of the DeepMIP database. *Geosci. Model Dev.* **12**, 3149–3206 (2019).

70. Kühl, N., Gebhardt, C., Litt, T. & Hense, A. Probability Density Functions as Botanical-Climatological Transfer Functions for Climate Reconstruction. *Quat. Res.* **58**, 381–392 (2002).

71. Greenwood, D.R., Keefe, R.L., Reichgelt, T. & Webb, J.A. Eocene paleobotanical altimetry of Victoria's Eastern Uplands. *Australian Journal of Earth Sciences* **64**, 625–637 (2017).

72. Harbert, R. S. & Nixon, K. C. Climate reconstruction analysis using coexistence likelihood estimation (CRACLE): A method for the estimation of climate using vegetation. *American Journal of Botany* **102**, 1277–1289 (2015).

73. GBIF. The Global Biodiversity Information Facility. What is GBIF?. Available from *https://www.gbif.org/what-is-gbif* [15.5.2019] (2019).

74. Fick, S.E. & Hijmans, R.J. WorldClim 2: new 1-km spatial resolution climate surfaces for global land areas. *Int. Journ. of Climatol.* **37**, 4302–4315 (2017).

75. Hijmans, R.J, Phillips, S., Leathwick, J. & Elith, J. Package 'dismo'. Available online at: *http://cran.r-project.org/web/packages/dismo/index.html* (2011).

76. Reichgelt, T., West, C. K. & Greenwood, D. R. The relation between global palm distribution and climate. *Scientific Reports* **8**, 4721 (2018).

77. Bourbonniere, R. A. & Meyers, P. A. Sedimentary geolipid records of historical changes in the watersheds and productivities of Lakes Ontario and Erie. *Limnology and Oceanography* **41**, 352–359 (1996).

78. Rütters, H. Sass, H., Cypionka, H. & Rullkötter, J. Phospholipid analysis as a toll to study complex microbial communities in marine sediments. *J. Microbiol. Meth.* **48**, 149–160 (2002).

79. Bauersachs, T., Talbot, H. M., Sidgwick, F., Sivonen, K. & Schwark, L. Lipid biomarker signatures as tracers for harmful cyanobacterial blooms in the Baltic Sea. *PLOS ONE* **12**, doi:10.1371/journal.pone.0186360 (2017).

80. Bauersachs, T., et al. Rapid analysis of long-chain glycolipids in heterocystous cyanobacteria using high-performance liquid chromatography coupled to electrospray ionization tandem mass spectrometry. *Rapid Comm. in Mass Spectrometry* **23**, 1387–1394 (2009).

81. Bauersachs, T., et al. Distribution of long chain heterocyst glycolipids in cultures of the thermophilic cyanobacterium *Mastigocladus laminosus* and a hot spring microbial mat. *Org. Geochem.* **56**, 19 – 24 (2013).

82. Wörmer, L., et al. Cyanobacterial heterocyst glycolipids in cultures and environmental samples: Diversity and biomarker potential. *Limnol. Oceanogr.* **57**, 1775–1788 (2012).

83. Schouten, S., et al. Endosymbiotic heterocystous cyanobacteria synthesize different heterocyst glycolipids than free-living heterocyst cyanobacteria. *Phytochemistry* **85**, 115–121 (2013).

84. Bale, N. J., et al. A novel heterocyst glycolipid detected in a pelagic N_2-fixing cyanobacterium of the genus *Calothrix*. *Org. Geochem.* **123**, 44–47 (2018).

85. Bauersachs, T., Miller, S. R., Gugger, M., Mudimu, O., Friedl, T. & Schwark, L. Heterocyte glycolipids indicate polyphyly of stigonematalean cyanobacteria. *Phytochem.* **166**, doi:10.1016/j.phytochem.2019.112059 (2019).

86. Ehrmann, W. et al. Provenance changes between recent and glacial-time sediments in the Amundsen Sea Embayment, West Antarctica: clay mineral assemblage evidence. *Antarctic Science* **23**, 471–486 (2011).

87. Petschick, R., Kuhn, G. & Gingele, F. Clay mineral distribution in surface sediments of the South Atlantic: sources, transport, and relation to oceanography. *Mar. Geol.* **130**, 203–229 (1996).

88. Kirschvink, J. L. The least-squares line and plane and the analysis of paleomagnetic data. *J. Royal Astr. Soc.* **62**, 699–718 (1980).

89. Roeckner, E., et al. The atmospheric general circulation model ECHAM 5. In: PARTI: Model Description, Report 349, Max-Planck-Institut für Meteorologie, Hamburg (2003).

90. Marsland, S.J., Haak, H., Jungclaus, J.H., Latif, M. & Roske, F. The Max-Planck-Institute global ocean/sea ice model with orthogonal curvilinear coordinates. *Ocean Model* **5**, 91–127 (2003).

91. Hagemann, S. & Dumenil, L. A parametrization of the lateral waterflow for the global scale. *Clim. Dyn.* **14**, 17–31 (1997).

92. Hibler III, W.D. A dynamic thermodynamic sea ice model. *J. Phys. Oceanogr.* **9**, 815–846 (1979).

93. Markwick, P.J. & Valdes, P.J. Palaeo-digital elevation models for use as boundary conditions in coupled ocean–atmosphere GCM experiments: a Maastrichtian (late Cretaceous) example. *Palaeogeogr. Palaeoclimatol. Palaeoecol.* **213**, 37–63 (2004).

94. Sewall, J.O., Van de Wal, R.S.W., Van Der Zwan, K., Van Oosterhout, C., Dijkstra, H.A. & Scotese, C.R. Climate model boundary conditions for four Cretaceous time slices. *Clim. Past* **3**, 647–657 (2007).

95. Niezgodzki, I., Tyszka, J., Knorr, G., & Lohmann, G. Was the Arctic Ocean ice free during the latest Cretaceous? The role of CO_2 and gateway configurations. *Global and Planetary Change* **177**, 201–212 (2019).

96. Wei, W. & Lohmann, G. Simulated Atlantic Multidecadal Oscillation during the Holocene. *J. Climate* **25**, 6989–7002 (2012).

97. Zhang, X., Lohmann, G., Knorr, G., & Purcell, C. Abrupt glacial climate shifts controlled by ice sheet changes. *Nature* **512**, 290–294 (2014).

98. Stepanek, C. & Lohmann, G. Modelling mid-Pliocene climate with COSMOS. *Geosci. Model Dev.* **5**, 1221–1243 (2012).

99. Knorr, G. & Lohmann, G. Climate warming during Antarctic ice sheet expansion at the Middle Miocene transition. *Nat. Geosci.* **7**, 376–381 (2014).

100. Stein, R. *et al.* Evidence for ice-free summers in the late Miocene central Arctic Ocean. *Nat. Comm.* **7**, 11148 (2016).

101. Walliser, E.O., Lohmann, G., Niezgodzki, I., Tütken,T. & Schöne, B.R. Response of Central European SST to atmospheric pCO2 forcing during the Oligocene – A combined proxy data and numerical climate model approach. *Palaeogeogr. Palaeoclimatol. Palaeoecol.* **459**, 552–569 (2016).

102. Vahlenkamp, M., et al. Astronomically Paced Changes in Deep-Water Circulation in the Western North Atlantic during the Middle Eocene. *Earth Planet. Sci. Lett.* **484**, 329–340 (2018).

103. Gierz, P., Lohmann, G. & Wei, W. Response of Atlantic Overturning to Future Warming in a coupled Atmosphere-Ocean-Ice Sheet Model. *Geophys. Res. Lett.* **42**, 6811–6818 (2015).

104. Simões Pereira, P., van de Flierdt, T., Hemming, S.R., Hammond, S.J., Kuhn, G., Brachfeld, S., Doherty, C. & Hillenbrand, C.D. Geochemical fingerprints of glacially eroded bedrock from West Antarctica: Detrital thermochronology, radiogenic isotope systematics and trace element geochemistry in Late Holocene glacial-marine sediments. *Earth-Science Rev.* **182**, 204-232 (2018).

105. Stacey, J. S. & Kramers, JD. Approximation of terrestrial lead isotope evolution by a two-stage model. *Earth Planet. Sci. Lett.* **26**, 207–221 (1975).

106. Chew, D. M., Sylvester, P. J. & Tubrett, M. N. U–Pb and Th–Pb dating of apatite by LA-ICPMS. *Chem. Geol.* **280**, 200–216 (2011).

107. O'Sullivan, G. J., Chew, D. M., Morton, A. C., Mark, C. & Henrichs, I. A. An Integrated Apatite Geochronology and Geochemistry Tool for Sedimentary Provenance Analysis. *Geochem. Geophys. Geosys.* **19**, 1309–1326 (2018).

108. Flowerdew, M.J., Tyrrell, S., Riley, T.R., Whitehouse, M.J., Mulvaney, R., Leat, P.T. & Marschall, H.R. Distinguishing East and West Antarctic sediment sources

using the Pb isotope composition of detrital K-feldspar. *Chem. Geol.* **292–293**, 88–102 (2012).

109. Petrus, J. A., & Kamber, B. S. VizualAge: A novel approach to laser ablation ICP MS U Pb geochronology data reduction. *Geostandards and Geoanalytical Research* **36**, 247–270 (2012).

110. Chew, D.M., Petrus, J. A. & Kamber, B. S. U-Pb LA-ICPMS dating using accessory mineral standards with variable common Pb. *Chem. Geol.* 363, 185–199 (2014).

111. C. Paton, Hellstrom, J., Paul, B.; Woodhead, J., Hergt, J. Iolite: freeware for the visualisation and processing of mass spectrometric data. *J. Anal. At. Spectrom.* **26**, 2508–2518 (2011).

112. Ludwig, K. R. User's manual for Isoplot 3.75: A geochronological Toolkit for Microsoft Excel. *Berkeley Geochronology Center Special Publication* **4**, 70 (2012).

113. Nasdala, L. et al. GZ7 and GZ8 - Two Zircon Reference Materials for SIMS U-Pb Geochronology. *Geostandards and Geoanalytical Research* **42**, 431–457 (2018).

114. McDowell, F. W., McIntosh, W. C. & Farley, K. A. A precise 40Ar–39Ar reference age for the Durango apatite (U–Th)/He and fission-track dating standard. *Chem. Geol.* **214**, 249–263 (2005).

115. Schoene, B. & Bowring, S. A. U–Pb systematics of the McClure Mountain syenite: thermochronological constraints on the age of the 40 Ar/39 Ar standard MMhb. *Contributions to Mineralogy and Petrology* **151**, 615 (2006).

116. Mark, C., Cogné, N. & Chew, D. Tracking exhumation and drainage divide migration of the western Alps: a test of the apatite U-Pb thermochronometer as a detrital provenance tool. *GSA Bulletin* **128**, 1439–1460 (2016).

117. Mao, M., Rukhlov, A.S., Rowins, S.M., Spence, J. & Coogan, L.A. Apatite trace element compositions: A robust new tool for mineral exploration. *Econom. Geol.* **111**, 1187–1222 (2016).

118. Woodhead, J.D., Hellstrom, J., Hergt, J.M., Greig, A. & Maas, R. Isotopic and elemental imaging of geological materials by laser ablation inductively coupled plasma-mass spectrometry. *Geostandards and Geoanalytical Research* **31**, 331–343 (2007).

Data availability

All data are available online in the *Data Base for Earth and Environmental Science* (PANGAEA) (DOI registration in progress). The dataset can be accessed via https://doi.pangaea.de/10.1594/PANGAEA.906092.

Code availability

The standard model code of the 'Community Earth System Models' (COSMOS) version COSMOS-landveg r2413 (2009) is available upon request from the 'Max Planck Institute for Meteorology' in Hamburg (https://www.mpimet.mpg.de). Analytical scripts are available in the PANGAEA database (https://doi.pangaea.de/10.1594/PANGAEA.910179).

Extended Data Figure 1: Tera-Wasserburg and PCA plots for uranium/lead (U/Pb) ages (in ±Myr). a) Tera-Wasserburg diagram showing apatite (red; 9.9 mbsf) and zircon (blue; 26.7 mbsf) U-Pb data. Red bar at upper array intercept for Eocene apatite is the range of crystalline basement $^{207}Pb_c/^{206}Pb_c$ values reported by (ref. 105) for West Antarctica, which anchor the apatite age calculation. Data-point error ellipses are 2σ. b) PCA plot showing trace-element data and single-grain ages for AWI-35 (9.9 mbsf) apatite, and lithological fields derived from bedrock apatite reference library[105]. Eocene grains (labelled in red) are chemically as well as chronologically distinct from other detrital apatite in the same sample. Data-point error ellipses are 2σ.

Extended Data Figure 2: Pollen abundance diagram. Percentages of most abundant pollen and spores and their total counts in cores 9R and 10R at site PS104_20-2.

Extended Data Figure 3: Photomicrographs of selected pollen and spores. a. *Cyathidites australis*; b. *Osmundacidites wellmanii*; c. *Ruffordiaspora australiensis*; d. *Ruffordiaspora ludbrookiae*; e. *Cycadopites follicularis*; f. *Microcachryidites antarcticus*; g. *Phyllocladidites mawsonii*; h. *Podocarpidites major*; i. *Trichotomosulcites hemisphaerius*; j. *Trichotomosulcites subgranulatus*; k. *Taxodiaceaepollenites hiatus*; l. *Equisetosporites sp.;* m. *Nyssapollenites chathamicus*; n. *Peninsulapollis gillii*; o. *Proteacidites subpalisadus.* All scale bars: 10 µm.

Extended Data Figure 4: Heterocyst glycolipid (HG) palaeothermometry. Presence of heterocyst glycolipids at 27.03–27.04 mbsf at site PS104_20-2 (core 9R) and river or lake surface water temperature (SWT) estimates from the heterocyst glycolipid-based molecular palaeothermometer.

Extended Data Figure 5: Example of microscopic images from thin sections. The sections are taken from a fossil root fragment between 29.34 and 29.43 mbsf in core 10R at site PS104_20-2. a) Overview scan of root fragment with indicated locations of detailed microscopic images b–e. White arrows indicate locations of preserved parenchyma storage cells including potential aerenchyma gas exchange cells (d). The scale bar in “d” applies to figures b–e.

Extended Data Figure 6: Biomarker presence. a) Pristane/n-C_{17} versus phytane/n-C_{18} to infer organic matter type during sediment deposition (after refs. 39, 40). b) Carbon preference index (CPI) and pristane/phytane (Pr/Ph) ratios. The CPI points to a low maturity and land plant origin of the organic matter (CPI > 1) deposited in an aquatic environment (Pr/Ph <2) and a peat swamp environment (Pr/Ph >2), respectively.

Extended Data Table 1: Percentages of most abundant pollen and spore taxa.

Extended Data Table 2: Selected key pollen taxa and NLR used to derive quantitative climate estimates.

Extended Data Table 3: Full list of identified pollen and spore taxa. All taxa identified during the current study are included. Question marks show uncertain taxa identifications, which require further studies. Those taxa marked with an asterisk have also been described from the Tupuangi Formation on the Chatham Islands[30,58].

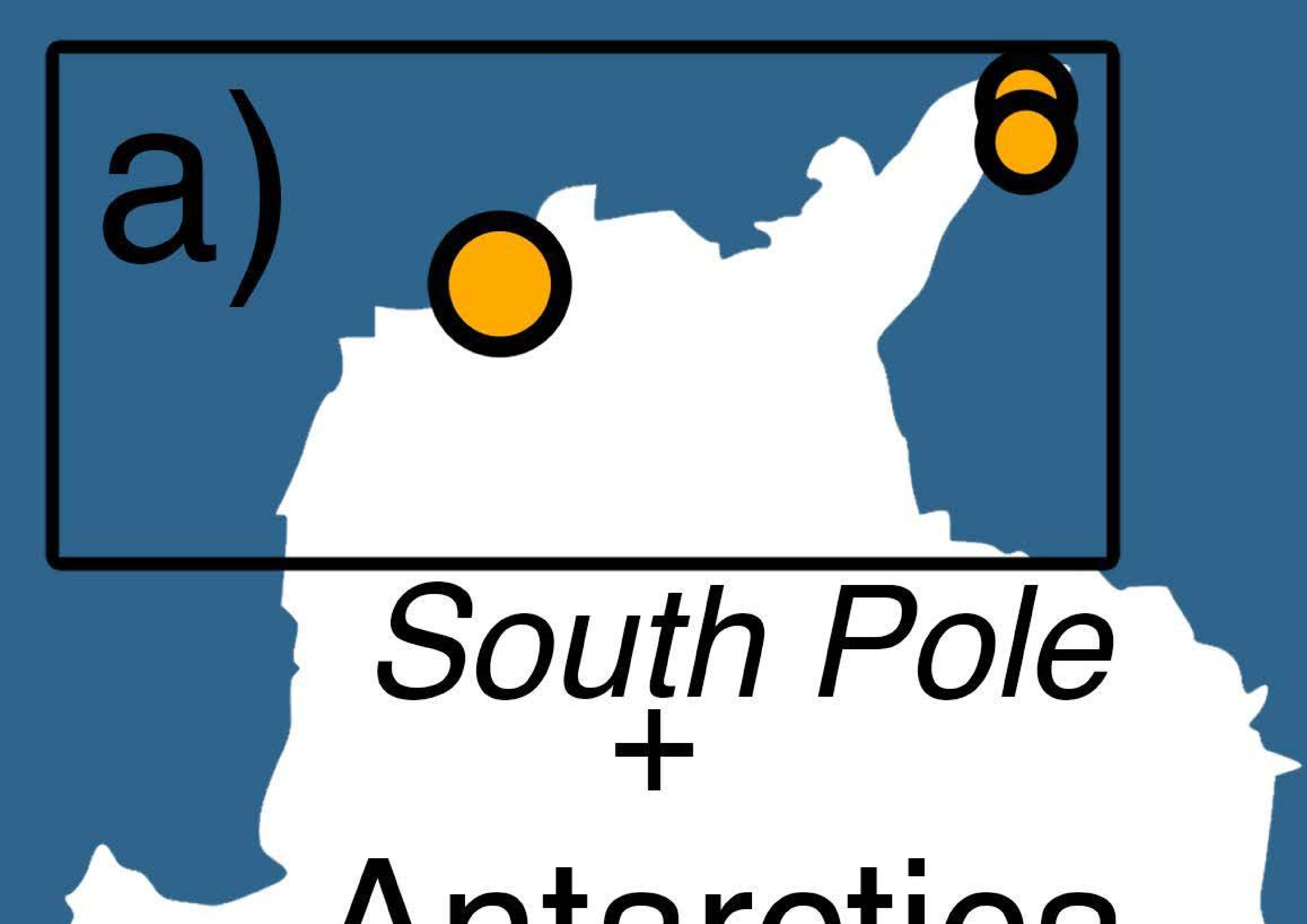
a)
South Pole
+

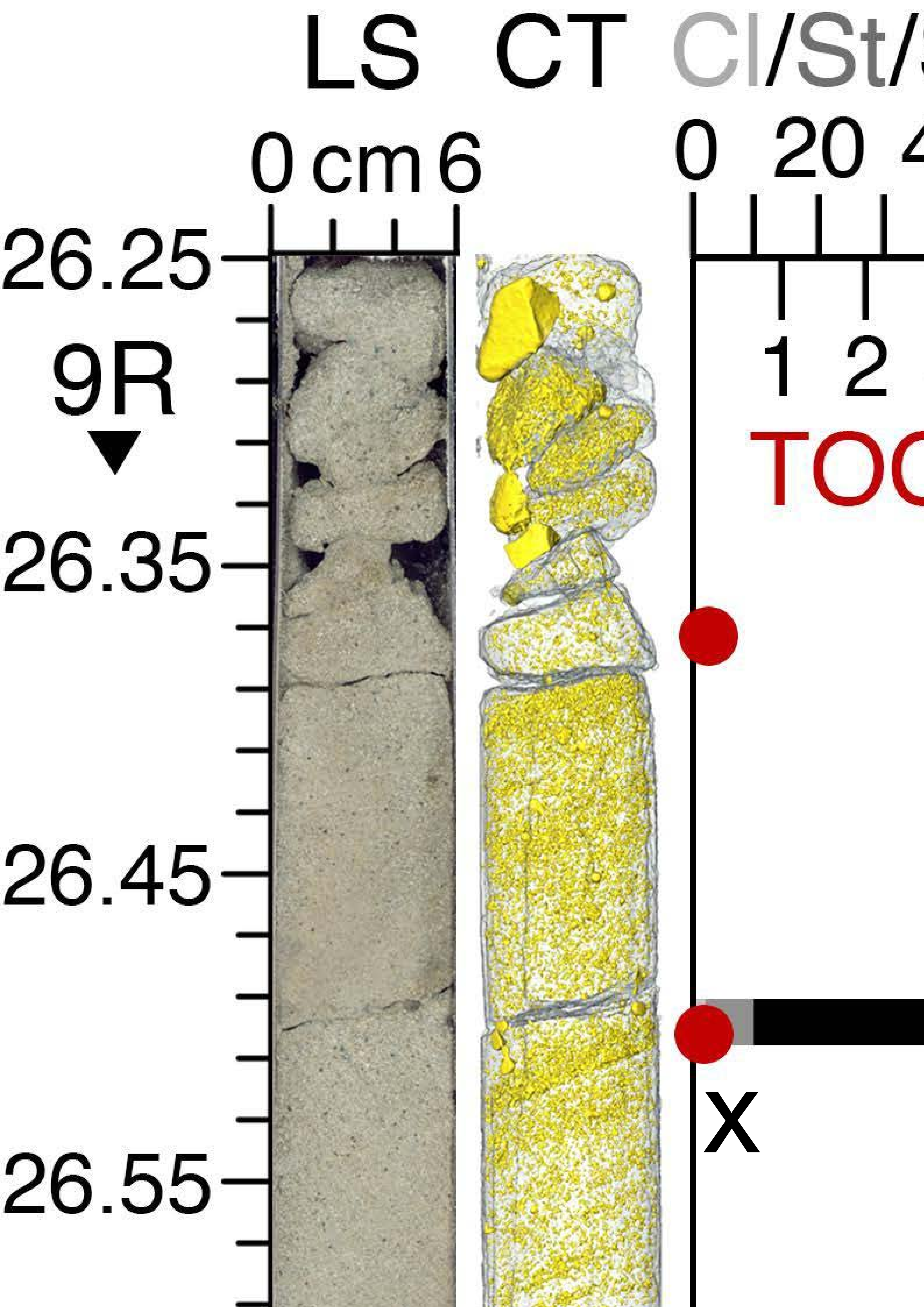

LS CT Cl/St/
0 cm 6
0 20 4
26.25
9R
1 2
TOC
26.35
26.45
X
26.55

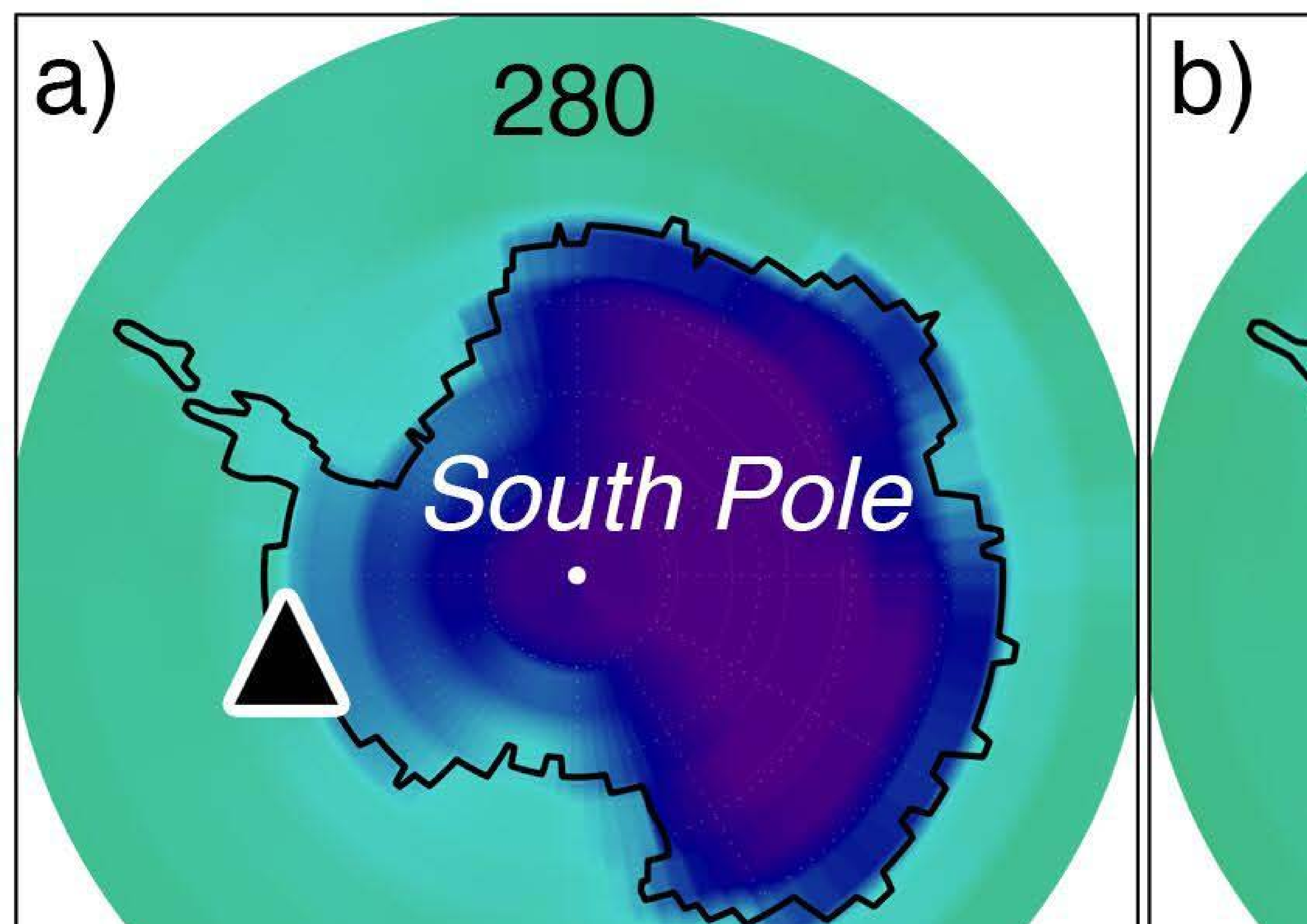
a)
280
South Pole
b)